Nonaxial shapes in the odd-odd ^{194}Au nucleus

B. S. Gao,[1,2,3] X. H. Zhou,[1,*] Y. D. Fang,[1] Y. H. Zhang,[1] S. C. Wang,[1,2] N. T. Zhang,[1] M. L. Liu,[1] J. G. Wang,[1] F. Ma,[1] Y. X. Guo,[1] X. G. Wu,[4] C. Y. He,[4] Y. Zheng,[4] Z. M. Wang,[4] S. C. Li,[1,2] X. L. Yan,[1,2] L. He,[1,2] Z. G. Wang,[1,2,3] Y. Zheng,[1] F. Fang,[1] and X. M. Chen[3]

[1]*Institute of Modern Physics, Chinese Academy of Sciences, Lanzhou 730000, People's Republic of China*
[2]*Graduate University of Chinese Academy of Sciences, Beijing 000049, People's Republic of China*
[3]*School of Nuclear Science and Technology, Lanzhou University, Lanzhou 730000, People's Republic of China*
[4]*China Institute of Atomic Energy, Beijing 102413, People's Republic of China*

High-spin states in the odd-odd ^{194}Au nucleus have been investigated using the ^{192}Os(^{7}Li, $5n$) reaction at a beam energy of 44 MeV. The previously known structures built on the $\pi h_{11/2}^{-1} \otimes \nu i_{13/2}^{-1}$ and $\pi h_{11/2}^{-1} \otimes \nu i_{13/2}^{-2} \nu j$ configurations are extended to high-spin states, and a new $I^\pi = (20^+)$ state associated with the $\pi h_{11/2}^{-1} \otimes \nu i_{13/2}^{-2} \nu h_{9/2}^{-1}$ configuration is identified. Importantly, the $\pi h_{11/2}^{-1} \otimes \nu i_{13/2}^{-1}$ band is found to exhibit normal signature splitting. The experimental results are compared with predictions from total Routhian surface and cranked shell-model calculations. Nonaxial shapes for the $\pi h_{11/2}^{-1} \otimes \nu i_{13/2}^{-1}$ and $\pi h_{11/2}^{-1} \otimes \nu i_{13/2}^{-2} \nu h_{9/2}^{-1}$ configurations are proposed. Possible reasons for the absence of signature inversion in the $\pi h_{11/2}^{-1} \otimes \nu i_{13/2}^{-1}$ band in ^{194}Au are discussed.

PACS number(s): 21.10.Re, 23.20.Lv, 25.70.Gh, 27.80.+w

I. INTRODUCTION

The gold isotopes located at the $A \sim 190$ transitional region show interesting shape coexistence and shape evolution phenomena, and their high-spin level structures have been extensively studied both experimentally and theoretically over the past years. Previous investigations suggested that the ground states in the light gold isotopes with $A \leqslant 187$ have near-prolate shapes [1]. However, triaxial deformations become evident with increasing neutron number. The low-lying states in the heavier Au isotopes have characteristics of triaxiality and γ softness [2–7], and the experimental signature inversion frequencies in the $\pi h_{11/2}^{-1} \otimes \nu i_{13/2}^{-1}$ bands of ^{188,190}Au were well reproduced by cranked shell-model (CSM) calculations in which nonaxial shape with $\gamma \leqslant -70°$ is assumed [5,7]. In order to study the shape-driving effects of the quasiparticles in the gold isotopes, total Routhian surface (TRS) calculations for ^{191}Au and the neighboring Pt nuclei were performed [6]. The results indicated that the Pt nuclei have γ-soft potential surfaces and the driving effects of the odd nucleons may be significant. The odd particle outside the even-even core exerts a strong driving force toward nonaxial shapes if a specific shape-driving orbital is occupied. To investigate the effect of nonaxiality on the level structures in Au nuclei, CSM calculations were carried out for ^{190,191}Au [5,6]. These calculations predicted that three lowest-lying positive-parity neutron Routhians (originating from the low-K $\nu i_{13/2}$ orbits) get close in energy at $\gamma \leqslant -80°$. Therefore, assuming large nonaxiality, one might expect the existence of three low-lying bands associated with the close-lying Routhians [6]. The experimental observations agree well with the predictions for the ^{190}Au isotope [5]. It will be interesting to extend the level scheme of ^{194}Au and to search for evidence for triaxial shape in this nucleus.

In this article we report the new experimental results on the high-spin structures in ^{194}Au. The experimental details and results are described in Sec. II and Sec. III, respectively. The detailed discussion of the high-spin properties of ^{194}Au is presented in Sec. IV. A brief summary is presented in Sec. V.

II. EXPERIMENTAL PROCEDURE

The nucleus ^{194}Au was produced using the ^{192}Os(^{7}Li, $5n$) reaction. The ^{7}Li beam was provided by the HI-13 tandem accelerator at the China Institute of Atomic Energy in Beijing (CIAE). The target was an isotopically enriched ^{192}Os metallic foil of 1.7 mg/cm^2 thickness with a 1.1 mg/cm^2 carbon backing. In order to optimize the production of ^{194}Au, the excitation function was measured at beam energies of 34, 38, 42, 44, and 46 MeV, and the beam energy of 44 MeV was chosen to populate the excited states in ^{194}Au. X-γ-t and γ-γ-t coincidence measurements were performed at the optimum beam energy. Here, t refers to the relative time difference between the two coincident γ rays, and X reffers to x rays. An array of 14 Compton-suppressed HPGe detectors was used to detect the γ rays emitted. The energy and efficiency calibrations were made using ^{60}Co, ^{133}Ba, and ^{152}Eu standard sources. Twenty γ lines of the standard sources were used in the calibrations. In order to estimate possible systematic errors for the measured γ-ray energies, we redetermined the γ-ray energy of each of the 20 standard γ rays by calibrating the spectrum with the other 19 γ rays. The systematic errors for the γ rays of the standard sources, defined as $\Delta E_\gamma = E_{\gamma,\mathrm{std}} - E_{\gamma,\mathrm{cal}}$, were then extracted from γ-ray energies $E_{\gamma,\mathrm{std}}$ of the standard sources adopted from the literature and $E_{\gamma,\mathrm{cal}}$ values obtained from the calibrations. For each of the γ-ray energies measured in our experiment, the systematic error was estimated by averaging the systematic errors for the γ rays of the standard sources around the γ-ray energy of interest. The systematic errors were approximately 0.1–0.6 keV depending on the energy

region. The energy resolutions of the Ge detectors were about 2.0–2.5 keV at full width at half maximum for the 1332.5-keV line. A total of 9×10^7 coincidence events were accumulated. After accurate gain matching, these coincidence events were sorted into a symmetric matrix for off-line analysis.

To obtain the multipolarity of the emitted γ rays, two asymmetric matrices were built using the detectors at all angles (y axis) against those located at θ_1 (40° and 152°) and θ_2 (90°) (x axes), respectively. From these two matrices, the angular

distribution asymmetry (ADO) ratios, defined as $R_{\mathrm{ADO}}(\gamma) = I_\gamma(\theta_1)/I_\gamma(\theta_2)$, were extracted from the γ-ray intensities $I_\gamma(\theta_1)$ and $I_\gamma(\theta_2)$ in the coincidence spectra gated by the transitions (on the y axis) of any multipolarity. A single gate was used for strong transitions. For some weak or doublet peaks, the gating transitions were carefully chosen to obtain clean coincidence spectra in which possible contaminations to the transitions of interest can be excluded. In the present geometry, stretched quadrupole transitions are adopted if $R_{\mathrm{ADO}}(\gamma)$ values are larger
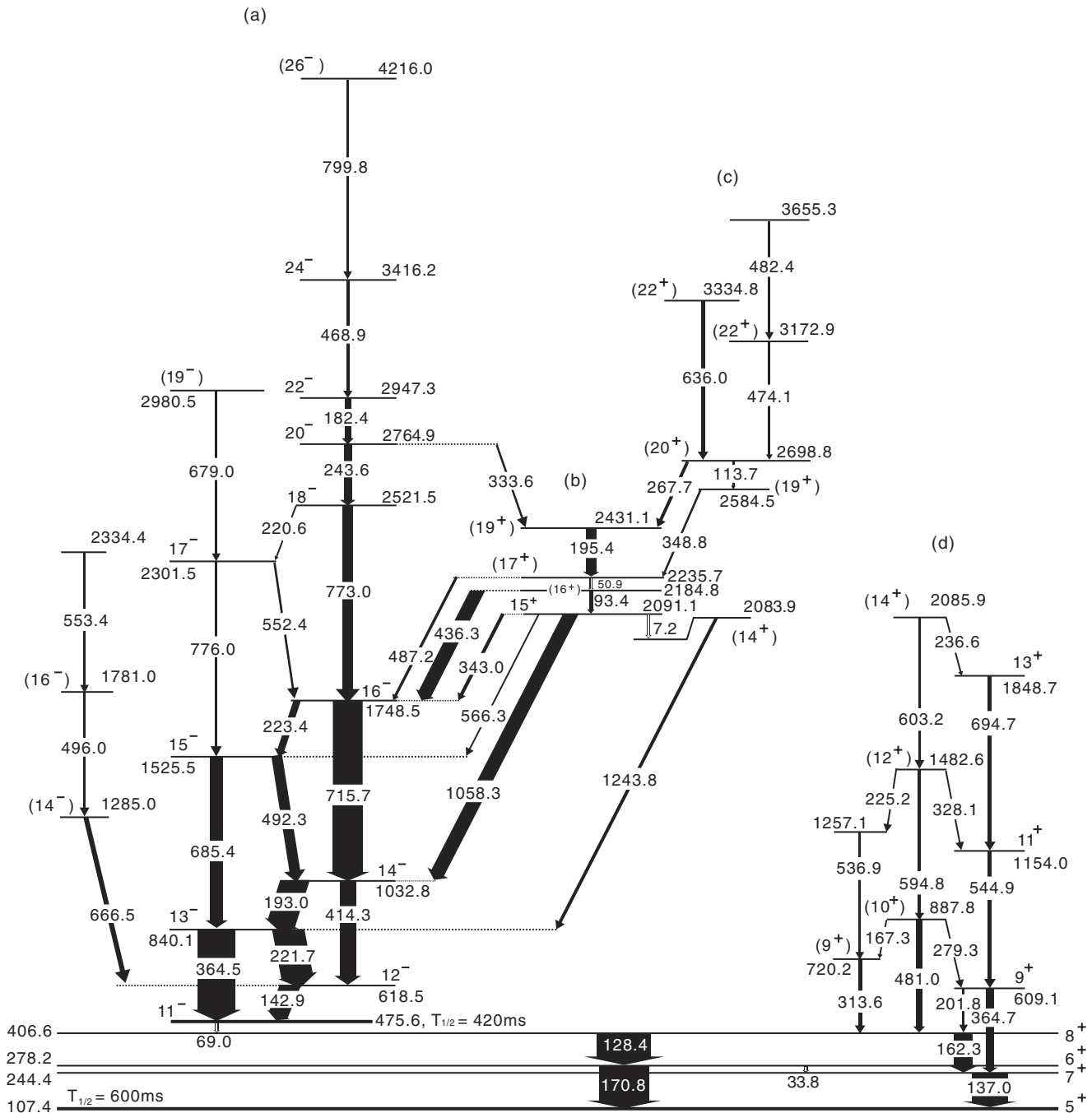

FIG. 1. Level scheme of ^{194}Au obtained from the present work. The excitation energies of levels are relative to the ground state and the levels below the 5^+ isomer are not shown in the scheme. The widths of the arrows represent the intensities of the transitions. Open arrows indicate transitions that are suggested from coincidence relationships.

TABLE I. γ-ray transition energies, relative intensities, angular distribution asymmetry ratios, and spin-parity assignments of the initial and final states in ^{194}Au. Uncertainties in energies and intensities are given in parentheses.

E_γ (keV)[a]	I_γ [b]	R_{ADO}	$E_i \to E_f$ (keV)[c]	$J_i^\pi \to J_f^\pi$ [d]
7.2(4)[e]			$2091.1 \to 2083.9$	$15^+ \to (14^+)$
33.8(2)[e]			$278.2 \to 244.4$	$6^+ \to 7^+$
50.9(7)	7(2)		$2235.7 \to 2184.8$	$(17^+) \to (16^+)$
93.4(2)	4(1)		$2184.8 \to 2091.1$	$(16^+) \to 15^+$
113.7(3)	<1		$2698.8 \to 2584.5$	$(20^+) \to (19^+)$
128.4(1)	143(9)		$406.6 \to 278.2$	$8^+ \to 6^+$
137.0(1)	96(6)		$244.4 \to 107.4$	$7^+ \to 5^+$
142.9(1)	53(3)		$618.5 \to 475.6$	$12^- \to 11^-$
162.3(1)	50(3)		$406.6 \to 244.4$	$8^+ \to 7^+$
167.3(3)	4(1)		$887.8 \to 720.2$	$(10^+) \to (9^+)$
170.8(1)	132(8)		$278.2 \to 107.4$	$6^+ \to 5^+$
182.4(2)	16(2)	1.25(14)	$2947.5 \to 2765.1$	$22^- \to 20^-$
193.0(1)	76(4)	0.82(9)	$1032.8 \to 840.1$	$14^- \to 13^-$
195.4(2)	28(2)	1.43(21)	$2431.1 \to 2235.7$	$(19^+) \to (17^+)$
201.8(3)	<3		$609.1 \to 406.6$	$9^+ \to 8^+$
220.6(3)	<2		$2521.5 \to 2301.5$	$18^- \to 17^-$
221.7(1)	85(7)	0.77(8)	$840.1 \to 618.5$	$13^- \to 12^-$
223.4(2)	19(3)	0.80(10)	$1748.5 \to 1525.5$	$16^- \to 15^-$
225.2(4)	<1		$1482.6 \to 1257.1$	$(12^+) \to$
236.6(3)	<2		$2085.9 \to 1848.7$	$(14^+) \to 13^+$
243.6(2)	21(3)	1.37(15)	$2765.1 \to 2521.5$	$20^- \to 18^-$
267.7(2)	9(2)	0.96(14)	$2698.8 \to 2431.1$	$(20^+) \to (19^+)$
279.3(2)	<3		$887.8 \to 609.1$	$(10^+) \to 9^+$
313.6(2)	9(2)	0.67(9)	$720.2 \to 406.6$	$(9^+) \to 8^+$
328.1(2)	<3		$1482.6 \to 1154.0$	$(12^+) \to 11^+$
333.6(2)	6(2)	0.66(8)	$2765.1 \to 2431.1$	$20^- \to (19^+)$
343.0(2)	9(2)	0.74(9)	$2091.1 \to 1748.5$	$15^+ \to 16^-$
348.8(2)	6(1)	1.37(21)	$2584.5 \to 2235.7$	$(19^+) \to (17^+)$
364.5(2)	100(9)	1.44(15)	$840.1 \to 475.6$	$13^- \to 11^-$
364.7(2)	21(3)	1.44(16)	$609.1 \to 244.4$	$9^+ \to 7^+$
414.3(3)	42(4)	1.44(16)	$1032.8 \to 618.5$	$14^- \to 12^-$
436.3(4)	37(3)	1.56(17)	$2184.8 \to 1748.5$	$(16^+) \to 16^-$
468.9(5)	8(2)	1.62(19)	$3416.4 \to 2947.5$	$24^- \to 22^-$
474.4(5)	6(1)	1.45(16)	$3172.9 \to 2698.8$	$(22^+) \to (20^+)$
481.0(5)	15(2)	1.38(16)	$887.8 \to 406.6$	$(10^+) \to 8^+$
482.4(6)	3(1)		$3655.3 \to 3172.9$	$\to (22^+)$
487.2(5)	7(2)	0.93(13)	$2235.7 \to 1748.5$	$(17^+) \to 16^-$
492.3(5)	29(2)	0.84(9)	$1525.5 \to 1032.8$	$15^- \to 14^-$
496.0(5)	5(1)	1.54(21)	$1781.0 \to 1285.0$	$(16^-) \to (14^-)$
536.9(6)	4(1)		$1257.1 \to 720.2$	$\to (9^+)$
544.9(5)	10(2)	1.51(17)	$1154.0 \to 609.1$	$11^+ \to 9^+$
552.4(5)	6(1)	1.42(20)	$2301.5 \to 1748.5$	$17^- \to 16^-$
553.4(6)	<1		$2334.4 \to 1781.0$	$\to (16^-)$
566.3(6)	7(1)		$2091.1 \to 1525.5$	$15^+ \to 15^-$
594.8(5)	7(1)	1.42(18)	$1482.6 \to 887.8$	$(12^+) \to (10^+)$
603.2(4)	6(1)	1.24(14)	$2085.9 \to 1482.6$	$(14^+) \to (12^+)$
636.0(4)	9(2)	1.49(17)	$3334.8 \to 2698.8$	$(22^+) \to (20^+)$
666.5(3)	13(1)	1.19(18)	$1285.0 \to 618.5$	$(14^-) \to 12^-$
679.0(5)	<3		$2980.5 \to 2301.5$	$(19^-) \to 17^-$
685.4(3)	35(4)	1.52(17)	$1525.5 \to 840.1$	$15^- \to 13^-$
694.7(4)	9(2)	1.41(17)	$1848.7 \to 1154.0$	$13^+ \to 11^+$
715.7(3)	80(4)	1.48(15)	$1748.5 \to 1032.8$	$16^- \to 14^-$
773.0(3)	29(2)	1.45(16)	$2521.5 \to 1748.5$	$18^- \to 16^-$
776.0(4)	6(1)		$2301.5 \to 1525.5$	$17^- \to 15^-$

TABLE I. *(Continued.)*

E_γ (keV)[a]	I_γ[b]	R_{ADO}	$E_i \rightarrow E_f$ (keV)[c]	$J_i^\pi \rightarrow J_f^{\pi}$ [d]
799.8(5)	<3		4216.2 → 3416.4	$(26^-) \rightarrow 24^-$
1058.3(2)	38(3)	0.87(9)	2091.1 → 1032.8	$15^+ \rightarrow 14^-$
1243.8(3)	9(2)	0.85(11)	2083.9 → 840.1	$(14^+) \rightarrow 13^-$

[a]The energy uncertainties are from the statistical error and the systematic error.
[b]Obtained from the γ-γ coincidence analysis and normalized to that of the 364.5-keV ($13^- \rightarrow 11^-$) transition. The intensity uncertainties include statistical errors and the contribution from the efficiency calibration.
[c]The excitation energies of the initial E_i and final E_f states.
[d]The proposed spin and parity assignments to the initial J_i^π and final J_f^π levels.
[e]Deduced from the coincidence relationships.

than unity (the average value of $R_{ADO}(\gamma)$ being approximately 1.40 ± 0.15 for the known $E2$ transitions in ^{194}Au), and dipole transitions are assumed if $R_{ADO}(\gamma)$ values are less than 1.0.

III. LEVEL SCHEME

Prior to the present work, many low-lying states in ^{194}Au were established through light-ion-induced reactions [8–10], and a rotational band built on the $\pi h_{11/2}^{-1} \otimes \nu i_{13/2}^{-1}$ configuration was observed up to the 2185-keV state [8]. Based on the coincidences with the known transitions, more than 30 new γ rays were assigned to ^{194}Au. On the basis of the analysis of γ-γ coincidence relationships, the level scheme of ^{194}Au has been extended up to $E_x = 4.2$ MeV in excitation energy and is presented in Fig. 1. Most of the previously reported transitions [8] were confirmed. The ordering of the transitions was determined according to the γ-γ coincidence relationships, γ-ray energy sums, and relative transition intensities. Spins were proposed to the excited states from the deduced ADO ratios. The measured γ-ray energies, γ intensities, and ADO ratios are listed in Table I.

Band (a) was most strongly populated, and it consists of a pair of signature partners. This band was associated with the $\pi h_{11/2}^{-1} \otimes \nu i_{13/2}^{-1}$ configuration and was known up to the 15^- and 16^- states in the previous work. The present work has extended the $\alpha = 0$ branch of band (a) from $I^\pi = 16^-$ to $I^\pi = (26^-)$ and the $\alpha = -1$ branch from $I^\pi = 15^-$ to $I^\pi = (19^-)$ (see Ref. [11] for the definition of the quantum number of signature α). In the previous work, the 2184.8-keV state was proposed to be the (17^-) state in band (a) [8]. Inspecting carefully the coincidence relationships of the transitions involved, we prefer the location of the 2184.8-keV state in structure (b) as discussed later. Representative spectra gated on transitions in band (a) are shown in Figs. 2 and 3, where most of the transitions in band (a) can be clearly seen. The ordering of transitions below the 2521.5-keV 18^- state was fixed firmly with the observation of intraband transitions. The placement of the 243.6-keV $20^- \rightarrow 18^-$ transition is rather certain due to the observation of a parallel 333.6-keV transition depopulating the 2765.1-keV 20^- state. As shown in Fig. 3, the 333.6-keV transition is in coincidence with the 414.3-, 715.7-, 182.4-, and 468.9-keV transitions but not with the 243.6- and 773.0-keV transitions. Moreover, the energy sums of the 243.6- and 773.0-keV transitions and the 487.2-, 195.4-, and 333.6-keV transitions are 1016.6(4) keV and 1016.2(6) keV, respectively; they are identical within the experimental uncertainties. The placement of the 182.4-, 468.9-, 799.8-, 776.0-, and 679.0-keV
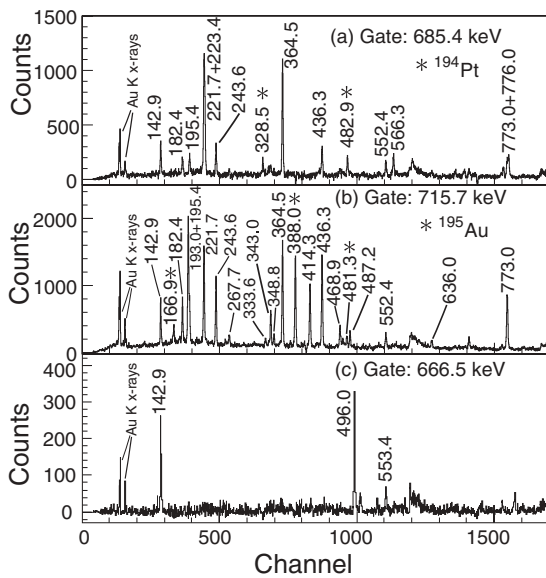

FIG. 2. γ-ray coincidence spectra gated on the (a) 685.4-keV transition, (b) 715.7-keV transition, and (c) 666.5-keV transition. Contaminations from ^{194}Pt and ^{195}Au are marked with asterisks.
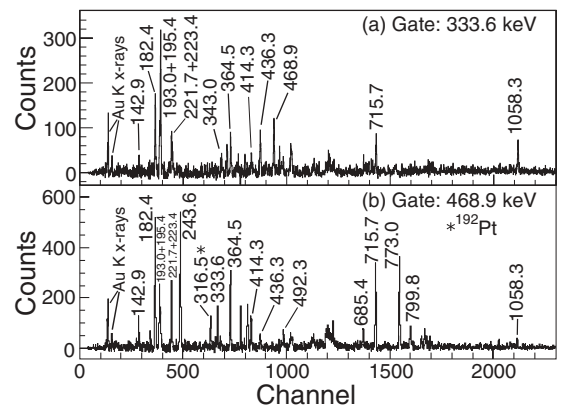

FIG. 3. γ-ray coincidence spectra gated on the (a) 333.6-keV transition and (b) 468.9-keV transition. Contamination from ^{192}Pt is marked with an asterisk.

transitions in the level scheme was based on their relative intensities. The ADO ratios extracted for the 243.6-, 182.4-, and 468.9-keV transitions are all consistent with the values expected for stretched $E2$ transitions, and therefore spin and parity values of 20^-, 22^-, and 24^- were assigned to the 2765.1-, 2947.5-, and 3416.4-keV levels, respectively. Additionally, a cascade of the 666.5-, 496.0-, and 553.4-keV transitions was observed, and this was proposed to feed the 618.5-keV state.

Structure (b) is built on the 2091.1-keV $I^\pi = 15^+$ state, which was identified in the previous work [8]. New 195.4-, 93.4-, 487.2-, and 566.3-keV transitions were observed in the present work. The 2184.8-keV state depopulated by the 436.3-keV transition was proposed to be the (17^-) state in band (a) [8]. By inspecting the spectra gated on the 436.3- and 1058.3-keV transitions shown in Figs. 4(a) and 4(b), it is obvious that the 436.3- and 1058.3-keV transitions are not in coincidence with the 243.6- and 773.0-keV transitions in band (a). Therefore, the 2184.8-keV state should not belong to band (a). Based on the coincidence patterns and energy sums of the transitions involved, the 2091.1-, 2184.8-, 2235.7-, and 2431.1-keV states were established. The measured ADO ratio for the 436.3-keV transition indicates that it is a stretched quadrupole transition or transition connecting levels with the same spin values, and thus we propose that the 2184.8-keV state should have a spin value of either 16 or 18. Considering the observation of the parallel 93.4-keV transition, we prefer

the assignment of a spin value of 16. Otherwise, the 93.4-keV transition should have an $M3$ multipolarity, and it could not compete with the 436.3-keV transition. The parallel 436.3- and 487.2-keV transitions feed the 16^- state at 1748.5 keV in band (a), and they show the same coincidence relationships with other transitions, as shown in Figs. 4(a) and 4(c). This suggests the existence of a 50.9-keV transition depopulating the 2235.7-keV state. In order to check the existence of the 50.9-keV transition, a nonsymmetrized matrix with all detectors against two low-energy photon detectors was constructed. The sum of the spectra gated on the 436.3- and 1058.3-keV transitions is shown in the inset of panel (b) in Fig. 4, where the 50.9-keV line can be clearly seen. The spin values for the 2235.7- and 2431.1-keV states were proposed from the ADO ratios deduced for the transitions concerned. The new 1243.8-keV transition was identified in the present work, and it was proposed to feed directly the 840.1-keV state. As shown in Fig. 4(d), the 1243.8-keV transition is in coincidence with the 142.9-, 221.7-, and 364.5-keV transitions in band (a) as well as the 195.4-keV transition in structure (b). For consistence, a low-energy 7.2-keV transition was assumed to connect the 15^+ 2091.1-keV and (14^+) 2083.9-keV states.

Structure (c) is built on the 2698.8-keV (20^+) state, which decays to the two (19^+) states. Spectra gated on the 267.7- and 348.8-keV lines are presented in Fig. 5, demonstrating the existence of structure (c). We assume positive parity for structure (c) based on the systematics of the level structures in the odd-odd Au nuclei. The assignment of spins to the levels in this structure was based on the ADO ratios deduced for the relevant transitions.

Band (d), consisting of three sequences, was weakly populated. The 364.7-, 544.9-, 694.7-, 313.6-, and 481.0-keV
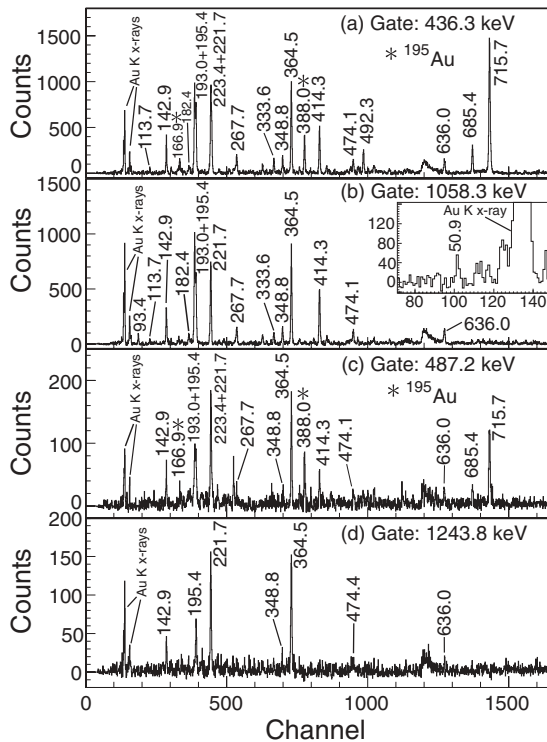

FIG. 4. γ-ray coincidence spectra gated on the (a) 436.3-keV transition, (b) 1058.3-keV transition, (c) 487.2-keV transition, and (d) 1243.8-keV transition. Contaminations from ^{195}Au are marked with asterisks. The inset in panel (b) is the sum of spectra gated on the 436.3- and 1058.3-keV transitions (see text).
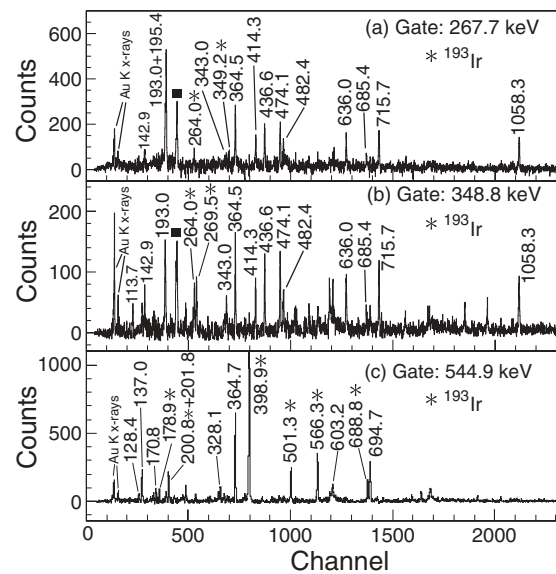

FIG. 5. γ-ray coincidence spectra gated on the (a) 267.7-keV transition, (b) 348.8-keV transition, and (c) 544.9-keV transition. The lines marked with solid squares are triplets composed of the 223.4-, 222.7- and 219.2-keV transitions, of which the 219.2-keV transition is contamination from ^{193}Ir. Other contaminations from ^{193}Ir are marked with asterisks.

transitions were observed in the previous work [8], and the other transitions were identified in the present work. Linking transitions between the sequences were also observed, which fixed the locations of transitions in band (d). Although the linking transitions are weak, their existence is evident, as shown in Fig. 5(c).

IV. DISCUSSION

Nonaxial shapes were suggested for odd-odd $^{186-192}$Au nuclei [5,7,12,13], and triaxial deformation might be expected for ^{194}Au from the structure similarities among the odd-odd Au isotopes. In order to get shape information for different configurations in ^{194}Au, we performed TRS calculations in the three-dimensional deformation β_2, β_4, and γ space [14]. The nonaxial deformed Woods-Saxon (WS) potential was employed [15]. Both monopole and quadrupole pairings were included [16,17]. To avoid the spurious pairing phase transition encountered in the BCS approach, we used the approximate particle number projection (Lipkin-Nogami pairing) [18]. The pairing correlation is dependent on rotational frequency ($\hbar\omega$) and deformation. To include such dependence in the TRS calculations, we carried out pairing-deformation-frequency self-consistent TRS calculations; i.e., for any given frequency and deformation, the pairing is self-consistently calculated by the Hartree-Fock-Bogoliubov (HFB)-like method [18]. At a given frequency, the deformation of a state is determined by minimizing the calculated TRS. Calculated TRS values for different configurations in ^{194}Au are plotted in Fig. 6, and the equilibrium shapes from TRS calculations are summarized in Table II (and configuration assignments will be discussed in the following sections).It can be seen from Fig. 6 that the configurations have large γ deformations. The nonaxiality of nuclear shapes may influence the relative positions of quasiparticle Routhians as demonstrated in ^{188,190,192}Au [5,7,12]. In order to study such effects, CSM calculations were performed for ^{194}Au using $\beta_2 = 0.13$ and $\beta_4 = -0.029$ as predicted by the TRS calculations, and by varying the γ value from $-60°$ to $-90°$. The calculated neutron quasiparticle Routhians are shown in Fig. 7, and detailed discussions will be presented in the following paragraphs. To facilitate the discussion of quasiparticle properties at high spins, we have labeled individual Routhians closest to the Fermi surface by letter designations. The correspondence among those labels,

TABLE II. Calculated equilibrium deformations from the TRS calculations for selected configurations in ^{194}Au at different rotational frequencies. Deformation parameters for ^{188}Au and ^{190}Au are taken from Ref. [7] and Ref. [5], respectively.

Nucleus	Configuration	α	$\hbar\omega$	β_2	γ
^{188}Au	$\pi h_{11/2}^{-1} \otimes \nu i_{13/2}^{-1}$	-1	0.20	0.16	$-83°$
^{188}Au	$\pi h_{11/2}^{-1} \otimes \nu i_{13/2}^{-1}$	0	0.20	0.16	$-69°$
^{190}Au	$\pi h_{11/2}^{-1} \otimes \nu i_{13/2}^{-1}$	-1	0.168	0.14	$-78°$
^{190}Au	$\pi h_{11/2}^{-1} \otimes \nu i_{13/2}^{-1}$	0	0.168	0.14	$-70°$
^{194}Au	$\pi h_{11/2}^{-1} \otimes \nu i_{13/2}^{-1}$	-1	0.166	0.13	$-79°$
^{194}Au	$\pi h_{11/2}^{-1} \otimes \nu i_{13/2}^{-1}$	0	0.166	0.13	$-71°$
^{194}Au	$\pi h_{11/2}^{-1} \otimes \nu i_{13/2}^{-2} \nu h_{9/2}^{-1}$	0	0.166	0.14	$-86°$

the parity and signature, and shell-model notations is outlined in Table III.

In order to discuss the band properties at high spins and study the effect of rotation on the independent particle motion in a deformed potential, it is necessary to transform the experimental excitation energies and spins into the rotating frame [19]. The standard plot of the aligned angular momentum and Routhian for bands (a) and (d) as a function of rotational frequency is shown in Fig. 8. These quantities are extracted from the measured spins, level energies, and transition energies according to Ref. [19]. The Harris parameters $J_0 = 8\hbar^2 \text{ MeV}^{-1}$ and $J_1 = 25\hbar^4 \text{ MeV}^{-3}$ are used, which give zero alignment for the ground-state band of the even-even ^{196}Hg nucleus [20].

A. Band (a)

In the previous work, the $\pi h_{11/2}^{-1} \otimes \nu i_{13/2}^{-1}$ configuration was assigned to band (a) [8]. In the notation of the CSM, the three sequences observed experimentally should correspond to the eA, eB, and eC configurations, respectively. From Fig. 8(a), we can see that band (a) displays normal signature splitting; the Routhian of the favored signature branch is lower in energy than that of the unfavored signature branch. However, low-spin signature inversion was systematically observed in the analogous $\pi h_{11/2}^{-1} \otimes \nu i_{13/2}^{-1}$ bands in odd-odd $^{188-192}$Au isotopes [2,5,7,12,13]. The signature inversion is manifested by the crossing of the Routhians at low rotational frequency; i.e., the Routhian of the unfavored signature branch lies lower in
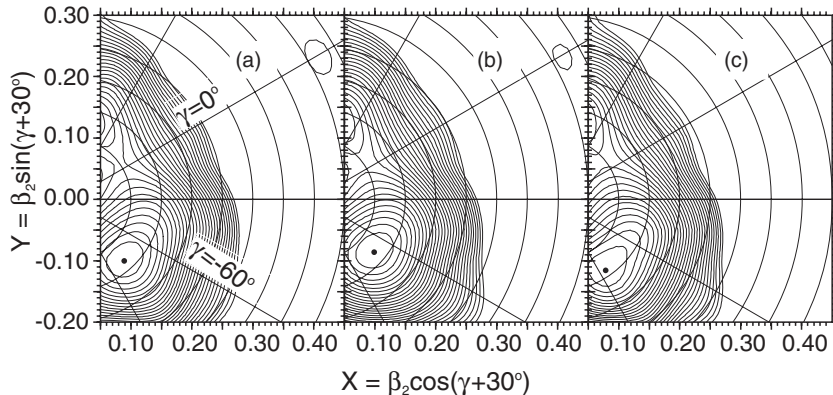

FIG. 6. TRS calculations for the configurations $\pi h_{11/2}^{-1} \otimes \nu i_{13/2}^{-1}$ ($\alpha = -1$ branch in left panel and $\alpha = 0$ branch in middle panel) and $\pi h_{11/2}^{-1} \otimes \nu i_{13/2}^{-2} \nu h_{9/2}^{-1}$ (right panel) in ^{194}Au. The calculations correspond to rotational frequency $\hbar\omega = 0.166$ MeV.
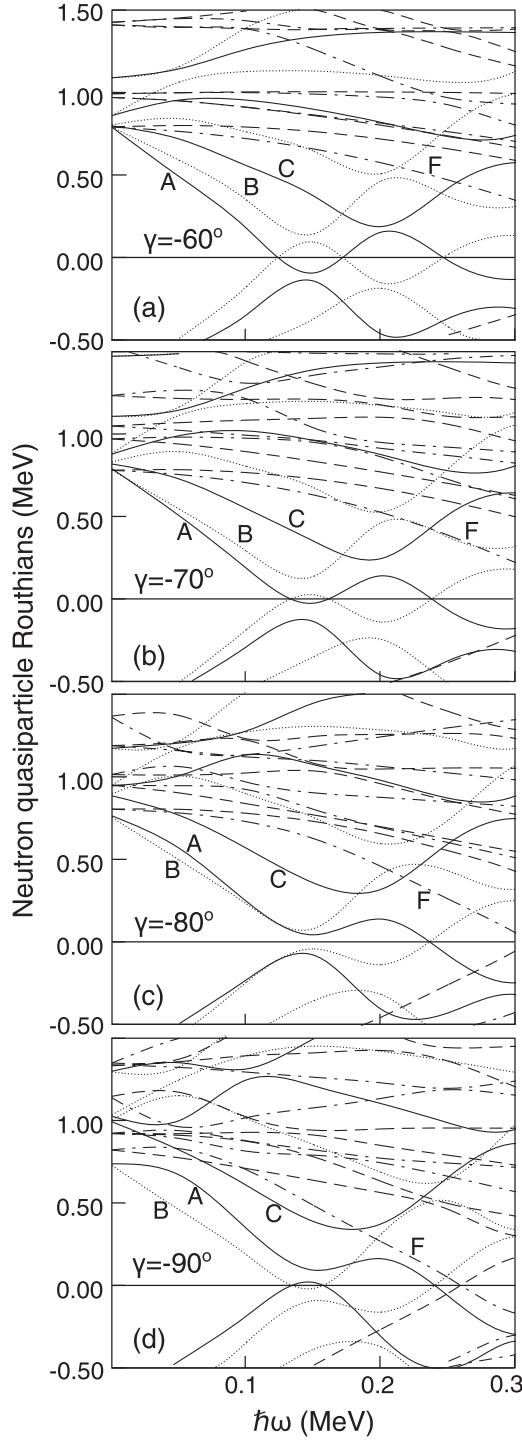
FIG. 7. Cranked shell-model calculations for ^{194}Au performed for neutrons. Nuclear deformations of $\beta_2 = 0.13$ and $\beta_4 = -0.029$ are chosen. The panels from top to bottom correspond to $\gamma = -60°$, $-70°$, $-80°$, and $-90°$. The Routhians with $(\pi, \alpha) = (+, +1/2)$ are represented with a solid line, $(+, -1/2)$ with a dotted line, $(-, +1/2)$ with a dash-dotted line, and $(-, -1/2)$ with a dashed line.

TABLE III. Definition of quasiparticle configurations and Routhian labels used in the text. Capital letters represent neutron excitations and lowercase letter represents proton excitation.

Routhian label	(π, α)	Dominant shell-model state
A	$(+, +1/2)$	$\nu i_{13/2}$
B	$(+, -1/2)$	$\nu i_{13/2}$
C	$(+, +1/2)$	$\nu i_{13/2}$
F	$(-, +1/2)$	$\nu h_{9/2}$
e	$(-, -1/2)$	$\pi h_{11/2}$

$-60°$ to $-90°$. Therefore, the signature splitting decreases quickly with decreasing γ value, and the signature inversion might occur at certain γ deformation. As shown in Fig. 7, the signature inversion might occur in the γ interval from $-80°$ to $-90°$ in ^{194}Au, but at $\sim -70°$ in ^{188,190}Au [5,7]. On the other hand, with increasing neutron number, the neutron Fermi surface gradually approaches the $\Omega = 1/2$ $i_{13/2}$ orbit, causing the enhancement of an admixture of the $\Omega = 1/2$ component into the wave function. Figure 9 presents plots of the signature splitting for the $\pi h_{11/2}^{-1} \otimes \nu i_{13/2}^{-1}$ bands in odd-odd $^{188-194}$Au [7, 12], defined as $S(I) = [E(I) - E(I-1)] - 1/2[E(I+1) - E(I) + E(I-1) - E(I-2)]$. Here $E(I)$ is the level energy of state I; $S(I)$ is directly proportional to the signature splitting Δe but is magnified by approximately a factor of 2. As shown in Fig. 9, the amplitude of signature splitting increases gradually in the $\pi h_{11/2}^{-1} \otimes \nu i_{13/2}^{-1}$ band from ^{188}Au to ^{194}Au. Therefore, the absence of signature inversion in ^{194}Au might be attributed to
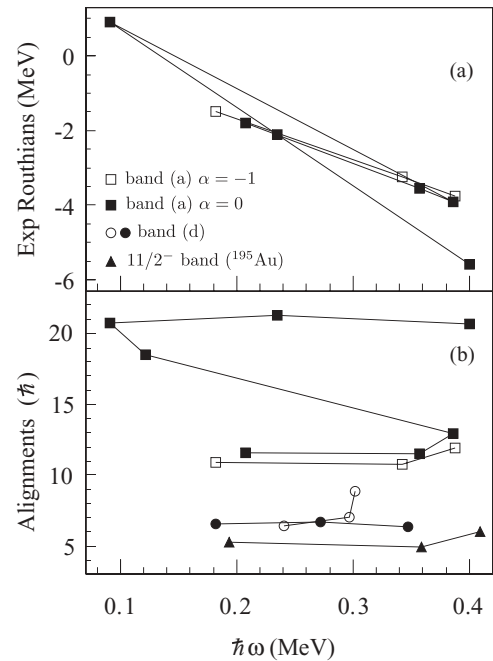

FIG. 8. Experimental Routhians and alignments for different bands. Data for the alignments of the $11/2^-$ band in ^{195}Au are taken from Ref. [25]. Harris parameters of $J_0 = 8\hbar^2$ MeV^{-1} and $J_1 = 80\hbar^4$ MeV^{-3} are chosen for band (d) to keep the alignments constant, and for other bands the Harris parameters are $J_0 = 8\hbar^2$ MeV^{-1} and $J_1 = 25\hbar^4$ MeV^{-3}, which give zero alignment for the ground-state band of the ^{196}Hg nucleus [20].

energy than that of favored signature branch, and the normal phase is restored at higher rotational frequency [2,5,7,12,13]. By inspecting Fig. 7, it can be seen that the B Routhian drops down and the A Routhian rises with decreasing γ value from
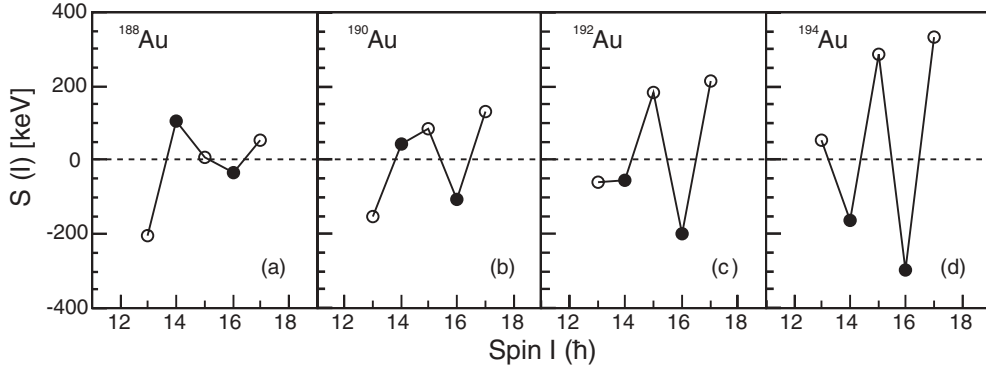
FIG. 9. Plot of signature splittings $S(I)$ vs I for the $\pi h_{11/2}^{-1} \otimes \nu i_{13/2}^{-1}$ bands observed in ^{194}Au and the corresponding bands in ^{188}Au [7] and ^{190,192}Au [12]. The solid (open) symbols correspond to the signature-favored (signature-unfavored) levels.

the insufficient triaxial deformation and large Coriolis-induced signature splitting.

In band (a), the two signature branches show rather large initial alignments of about $11\hbar$ and $12\hbar$, and they behave similarly at low rotational frequency. With the addition of new transitions on the top of band (a), a band crossing at $\hbar\omega \approx 0.23$ MeV is observed for the favored signature branch. We propose that the band crossing is caused by the alignment of a pair of $i_{13/2}$ neutrons, and thus the band above the crossing has a $\pi h_{11/2}^{-1} \otimes \nu i_{13/2}^{-3}$ configuration. The alignment gain of about $10.0\hbar$ after the crossing is consistent with the $i_{13/2}$ neutron alignment. As shown in Fig. 7, the band crossing can be reproduced by the calculations. The $i_{13/2}$ neutron alignment was observed systematically in the neighboring ^{194,196}Hg [21,22], ^{192}Pt [23,24], and ^{190,191,193}Au [3–6] isotopes.

B. Structure (b) built on the 15$^+$ state

Semidecoupled bands built on the 15$^+$ states in ^{188,190,192}Au were observed experimentally, and the $\pi h_{11/2}^{-1} \otimes \nu i_{13/2}^{-2}\nu j$ (j being $p_{3/2}$ or $f_{5/2}$) configuration was assigned to the 15$^+$ states [5,7,12]. The 15$^+$ state at 2091.1 keV should be the analogous state in ^{194}Au. By comparing the structures associated with the 15$^+$ states in the odd-odd Au isotopes, some differences can be found. For instance, a strong $17^+ \rightarrow 15^+$ $E2$ transition was observed in $^{188-192}$Au while the transition from (17^+) to 15$^+$ in ^{194}Au is missing, and the (20^+) states with configuration of $\pi h_{11/2}^{-1} \otimes \nu i_{13/2}^{-2}\nu h_{9/2}^{-1}$ in $^{188-192}$Au decay through two $E2$ transitions to the 18$^+$ levels while the (20^+) state decays by two $M1$ transitions to the (19^+) states in ^{194}Au. These findings suggest that the intrinsic structure of the 15$^+$ and 20$^+$ states in the odd-odd Au isotopes might be different. The difference is probably caused by the different γ deformations of these states.

C. The (20$^+$) state at 2698.8 keV in structure (c)

The 2698.8-keV (20^+) state should have a four-quasiparticle configuration. By considering the orbits close to the Fermi surface in ^{194}Au, a $\pi h_{11/2}^{-1} \otimes \nu i_{13/2}^{-2}\nu h_{9/2}^{-1}$ configuration might be associated with the (20^+) state at 2698.8 keV. The

$I^\pi = 20^+$ states with configuration of $\pi h_{11/2}^{-1} \otimes \nu i_{13/2}^{-2}\nu h_{9/2}^{-1}$ were systematically observed in ^{186,188,190,192}Au [7,12,13]. Inspecting the level schemes of the odd-odd Au isotopes, we can find that the 20$^+$ states have close excitation energies (relative to the 11$^-$ states) and similar decay patterns. This indicates that these 20$^+$ states may have the same configuration, supporting the assignment of the same configuration to the (20^+) level in ^{194}Au. We would like to point out that the 20$^+$ and 20$^-$ states have approximately the same excitation energy in ^{194}Au, but the excitation energy of the 20$^+$ state is $\sim$0.6 MeV lower than that of the 20$^-$ state in ^{190}Au. The 20$^+$ and 20$^-$ states in the odd-odd Au isotopes have $\pi h_{11/2}^{-1} \otimes \nu i_{13/2}^{-2}\nu h_{9/2}^{-1}$ and $\pi h_{11/2}^{-1} \otimes \nu i_{13/2}^{-3}$ configurations, respectively. The TRS calculations predicted nearly identical nonaxiality of $\gamma \sim -90°$ for the (20^+) states in ^{190,194}Au (see Fig. 6(c) and Ref. [5]). However, the influence of γ deformation on the F Routhian (originating from the $\nu h_{9/2}$ subshell) seems to be different in ^{194}Au and in ^{190}Au. It can be seen from Fig. 7(d) that in ^{194}Au the F Routhian lies higher in energy than the A, B, and C Routhians having the parentage of $\nu i_{13/2}$. On the other hand, the F Routhian lies close in energy with the A, B, and C Routhians at $\gamma \sim -90°$ in ^{190}Au, as shown in Fig. 7 in Ref. [5]. This might be the reason for the energy difference.

D. Band (d)

Band (d) is built on the low-spin states with configuration of $\pi d_{3/2}^{-1} \otimes \nu i_{13/2}^{-1}$ [10]. The three sequences observed experimentally might involve the A, B, and C orbits having the parentage of $\nu i_{13/2}^{-1}$, respectively. Figure 8 shows alignments for the sequences consisting of the 364.7-, 544.9-, and 694.7-keV transitions and the 481.0-, 594.8-, and 603.2-keV transitions. In order to keep the alignments constant, Harris parameters of $J_0 = 8\hbar^2$ MeV^{-1} and $J_1 = 80\hbar^4$ MeV^{-3} are used. As shown in Fig. 8, band (d) has an initial alignment of about $\sim$7$\hbar$, which is about 4$\hbar$ less than that of the band built on the $\pi h_{11/2}^{-1} \otimes \nu i_{13/2}^{-1}$ configuration. This is reasonable since the $d_{3/2}$ proton orbit has a smaller j value. For comparison, the alignment of the $\pi h_{11/2}$ band in the neighboring ^{195}Au nucleus is also presented in Fig. 8. This band has an initial alignment of $\sim$5.5$\hbar$. The $\pi d_{3/2}^{-1} \otimes \nu i_{13/2}^{-1}$ and $\pi h_{11/2}^{-1} \otimes \nu i_{13/2}^{-1}$ configurations should have

the same neutron alignments, and the alignment difference is caused by the proton contributions.

V. SUMMARY

In summary, high-spin states in ^{194}Au have been studied using the ^{192}Os(^{7}Li, $5n$) reaction. The previously known structures based on the $\pi h_{11/2}^{-1} \otimes \nu i_{13/2}^{-1}$, $\pi h_{11/2}^{-1} \otimes \nu i_{13/2}^{-2}\nu j$, and $\pi d_{3/2}^{-1} \otimes \nu i_{13/2}^{-1}$ configurations have been extended, and a new $I^\pi = (20^+)$ state associated with the $\pi h_{11/2}^{-1} \otimes \nu i_{13/2}^{-2}\nu h_{9/2}^{-1}$ configuration has been identified. TRS calculations showed that the signature partners of the $\pi h_{11/2}^{-1} \otimes \nu i_{13/2}^{-1}$ band have pronounced nonaxial shapes. The absence of signature inversion in the $\pi h_{11/2}^{-1} \otimes \nu i_{13/2}^{-1}$ band can be attributed to the insufficient triaxial deformation and large Coriolis-induced signature splitting. The calculated neutron quasiparticle Routhians sug-gest that, at large γ deformation, the F Routhian originating from the $\nu h_{9/2}$ subshell lies high in energy in ^{194}Au, which might explain the relatively higher excitation energy of the 20^+ state with configuration of $\pi h_{11/2}^{-1} \otimes \nu i_{13/2}^{-2}\nu h_{9/2}^{-1}$ in ^{194}Au. The experimental results presented in this work extend our knowledge of high-spin states in the heavy odd-odd Au isotopes.

[1] P. Joshi, A. Kumar, G. Mukherjee, R. P. Singh, S. Muralithar, U. Garg, R. K. Bhowmik, and I. M. Govil, Phys. Rev. C **66**, 044306 (2002), and references therein.

[2] V. P. Janzen *et al.*, Phys. Rev. C **45**, 613 (1992).

[3] Y. Oktem *et al.*, Phys. Rev. C **76**, 044315 (2007).

[4] Y. Oktem *et al.*, Phys. Rev. C **78**, 069904(E) (2008).

[5] E. Gueorguieva, C. Schück, A. Minkova, Ch. Vieu, M. Kaci, F. Hannachi, R. Wyss, J. S. Dionisio, A. Korichi, and A. Lopez-Martens, Phys. Rev. C **69**, 044320 (2004).

[6] E. Gueorguieva, C. Schuck, A. Minkova, C. Vieu, F. Hannachi, M. Kaci, M. G. Porquet, R. Wyss, J. S. Dionisio, A. Korichi, and A. Lopez-Martens, Phys. Rev. C **68**, 054308 (2003).

[7] Y. D. Fang *et al.*, Phys. Rev. C **82**, 064303 (2010).

[8] A. Neskakis, R. M. Lieder, H. Beuscher, Y. Gono, D. R. Haenni, and M. Müller-Veggian, Nucl. Phys. A **390**, 53 (1982).

[9] S. W. Yates and F. J. Lynch, Phys. Rev. C **12**, 1080 (1975).

[10] A. Pakkanen, M. Piiparinen, M. Kortelahti, T. Komppa, R. Komu, and J. Äystö, Z. Phys. A **282**, 277 (1977).

[11] Y. H. Zhang, M. Oshima, Y. Toh, X. H. Zhou, M. Koizumi, A. Osa, A. Kimura, Y. Hatsukawa, T. Morikawa, M. Nakamura, M. Sugawara, H. Kusakari, T. Komatsubara, K. Furuno, H. L. Wang, P. Luo, C. S. Wu, and F. R. Xu, Phys. Rev. C **68**, 054313 (2003).

[12] E. Gueorguieva *et al.*, Phys. Rev. C **64**, 064304 (2001).

[13] S. C. Li *et al.*, Chin. Phys. Lett. **29**, 022102 (2012).

[14] W. Nazarewicz, R. Wyss, and A. Johnson, Phys. Lett. B **225**, 208 (1989).

[15] W. Nazarewicz, J. Dudek, R. Bengtsson, and I. Ragnarsson, Nucl. Phys. A **435**, 397 (1985).

[16] W. Satula and R. Wyss, Phys. Rev. C **50**, 2888 (1994).

[17] F. R. Xu, W. Satula, and R. Wyss, Nucl. Phys. A **669**, 119 (2000).

[18] W. Satula, R. Wyss, and P. Magierski, Nucl. Phys. A **578**, 45 (1994).

[19] R. Bengtsson and S. Frauendorf, Nucl. Phys. A **327**, 139 (1979).

[20] D. Mehta *et al.*, Z. Phys. A **339**, 317 (1991).

[21] H. Hübel, A. P. Byrne, S. Ogaza, A. E. Stuchbery, G. D. Dracoulis, and M. Guttormsen, Nucl. Phys. A **453**, 316 (1986).

[22] R. Kroth, S. K. Bhattacherjee, C. Günther, M. Guttormsen, K. Hardt, H. Hübel, and A. Kleinrahm, Phys. Lett. B **97**, 197 (1980).

[23] J. C. Cunnane, M. Piiparinen, P. J. Daly, C. L. Dors, T. L. Khoo, and F. M. Bernthal, Phys. Rev. C **13**, 2197 (1976).

[24] S. A. Hjorth, A. Johnson, Th. Lindblad, L. Funke, P. Kemnitz, and G. Winter, Nucl. Phys. A **262**, 328 (1975).

[25] S. C. Wang *et al.*, Phys. Rev. C **85**, 027301 (2012).